Available online at www.sciencedirect.com

ScienceDirect

Mendeleev Commun., 2024, **34**, 643–646

Mendeleev Communications

Sol–gel prepared ZnO: UV irradiation effect on structure and surface properties

Ivan V. Sukhov,[a] Ivan A. Filippov,[a] Igor A. Pronin,*[a] Victor V. Sysoev,*[b] Valeriy M. Kondratev,[c,d] Alexei S. Komolov,[e] Eleonora F. Lazneva,[e] Andrey A. Karmanov,[a] Nadezhda D. Yakushova,[a] Vyacheslav A. Moshnikov[f] and Ghenadii Korotcenkov[g]

[a] *Department of Nano- and Microelectronics, Penza State University, 440026 Penza, Russian Federation. Fax: +7 8412 208393; e-mail: pronin_i90@mail.ru*
[b] *Department of Physics, Yuri Gagarin State Technical University of Saratov, 410054 Saratov, Russian Federation. Fax: +7 8452 998624; e-mail: vsysoev@sstu.ru*
[c] *Moscow Institute of Physics and Technology, 141701 Dolgoprudny, Moscow Region, Russian Federation*
[d] *Alferov University, 194021 St. Petersburg, Russian Federation*
[e] *St. Petersburg State University, 199034 St. Petersburg, Russian Federation*
[f] *St. Petersburg Electrotechnical University 'LETI', 197022 St. Petersburg, Russian Federation*
[g] *Department of Physics and Engineering, Moldova State University, 2009 Chisinau, Moldova*

DOI: 10.1016/j.mencom.2024.09.006

The effect of UV irradiation on sol–gel prepared ZnO films subjected to mild thermal annealing was investigated, with special attention to their structural and surface properties. Sol–gel processes, including a high-temperature annealing stage, have been adapted to the requirements of flexible electronics for *in situ* synthesis of semiconductor ZnO films on polymer substrates at lower temperatures due to UV irradiation. Application of UV radiation with emission peaks at 185 and 254 nm to films annealed at 180 °C made it possible to obtain ZnO films with Zn/O ratios of *ca.* 1, which cannot be achieved by heat treatment alone.

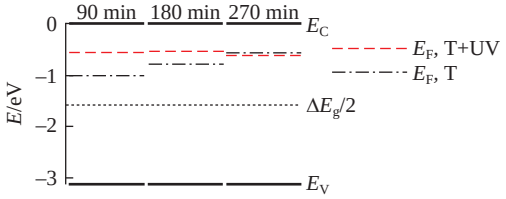

Keywords: sol–gel technology, epidermal electronics, zinc oxide, UV irradiation effect, XPS.

Wearable electronics is a new class of flexible electronic systems in which the thickness, effective modulus of elasticity, bending stiffness and density of functional films correspond to the human epidermis. By means of conformal contact and excellent adhesion to the skin, this type of technology can be widely used to measure the electrical activity of the brain and heart, as well as to create wearable sensing systems.[1–3] It is worth noting that these wearable sensor technologies are becoming increasingly relevant for personalized medicine due to the possibility of continuous monitoring of human health. Thus, such flexible sensors can provide continuous monitoring of various human physiological biomarkers in real time.[4–6]

A promising material for the flexible sensor devices is zinc oxide. Due to its high specific surface area, low cost, chemical stability, low toxicity, biocompatibility and semiconductor properties, it has the capacity to be modified at the surface, immobilize a biomatrix on it and generate a detectable analytical signal.[7] For instance, the development of a flexible electrochemical human sweat glucose biosensor with a reliable limit of detection of 1 mg dm^{-3} using a porous polyamide substrate with a thin Au/ZnO coating has been reported.[8] In another case, a cholesterol biosensor based on porous tubular zinc oxide was developed, which had a high sensitivity of 54 mA mol^{-1} cm^{-2} and a low limit of detection of 0.2 mmol when operating at room temperature.[9] Similar works, which have received due review recently, show that ZnO layers prepared as polycrystalline films, nanoparticles and nanowires are among the most promising materials for biosensor fabrication due to their improved sensing properties, enhanced biomolecule binding capacity and high biological activity.[10]

Sol–gel technology is an inexpensive and simple method for producing zinc oxide films, which allows precise control of the dispersion of the product, as well as flexible control of its nanostructure. This method of producing carriers for bioanalytical devices is extremely relevant: the sol–gel process makes it possible to obtain a micro-, meso- and macroporous three-dimensional ZnO matrices with a large surface area. This creates the opportunity to deposit a large number of biomatrix molecules on the surface of the carrier, avoiding its leaching.[11] Through a hierarchical pore system, analyte molecules diffuse from solution to the receptor molecule and at the same time the products of redox reactions are removed. However, the annealing step at relatively high temperatures when preparing metal oxide nanomaterials by the sol–gel method significantly limits its use together with polymer substrates in flexible and epidermal electronics. Therefore, the application of UV photochemical activation of sol–gel films at room temperature for the synthesis of functionally stable metal oxides, proposed in pioneering studies, opens up new applications for sol–gel protocols.[12] It has been shown that UV irradiation causes effective condensation and densification of oxide semiconductor films upon photochemical activation at low temperature. This technique is applicable to numerous metal oxide semiconductors,

© 2024 Mendeleev Communications. Published by ELSEVIER B.V. on behalf of the N. D. Zelinsky Institute of Organic Chemistry of the Russian Academy of Sciences.

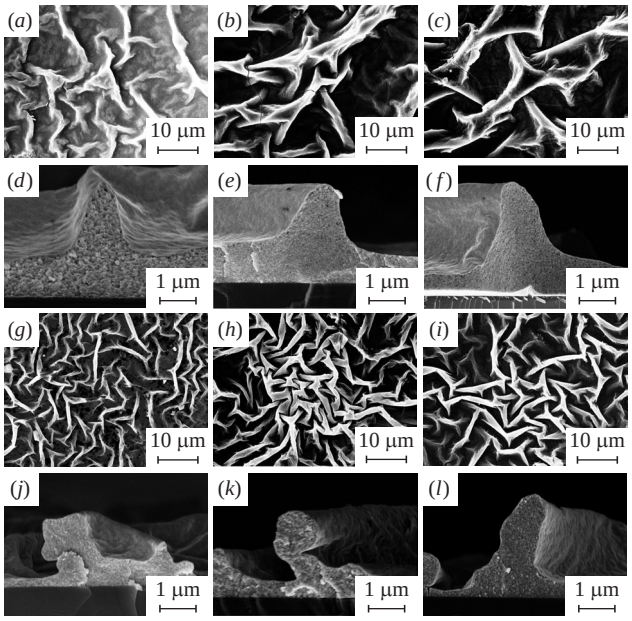

Figure 1 SEM images of the (*a*)–(*c*),(*g*)–(*i*) surface and (*d*)–(*f*),(*j*)–(*l*) cross section of the studied ZnO samples (*a*),(*d*) 90 T, (*b*),(*e*) 180 T, (*c*),(*f*) 270 T, (*g*),(*j*) 90 T+UV, (*h*),(*k*) 180 T+UV and (*i*),(*l*) 270 T+UV.

including ZnO. However, a review of modern research shows the absence of any data on the physicochemical conditions for the formation of sol–gel films on flexible substrates at low temperatures. In this work, we compare and investigate the formation of thin ZnO films at low temperatures by the sol–gel method with and without UV irradiation during the annealing process.

Figure 1 shows micrographs of the surface and cross section of all obtained samples. Details of the synthesis and physical characterization of the samples are given in Online Supplementary Materials. In all cases, zinc oxide forms films with a folded structure consisting of nanocrystallites. This morphology can be explained by the evaporation of the liquid phase during film annealing, leading to a decrease in its thickness. In this case, the remaining solid phase, concentrating as the volume of the film reduces, forms folds, since the contact area of the coating with the substrate remains unchanged. Probably, the main parameter influencing the size of the resulting fold is the rate of evaporation of the liquid phase: the lower the rate, the more equilibrium conditions the relaxation of the resulting mechanical stresses occurs, which leads to less curvature of the fold and, accordingly, a larger transverse size.

Analysis of the SEM images leads to the following reasonable conclusions. (i) In all cases, the thickness of films obtained by a combined method of mild heat treatment and UV radiation is less than the thickness of films obtained only by mild heat treatment without additional exposure to UV radiation. In the first case, their values are in the range of 300–500 nm, while in the second case, they are 1–1.5 μm. (ii) The transverse size of folds in films obtained by combined treatment is approximately 1–2 μm, which is also less than the values of 3–5 μm observed in the control samples. (iii) The height of the film folds in the samples subjected to combined treatment significantly exceeds the film thickness. In the case of control samples, the height of the fold is commensurate with the thickness of the film. (iv) Film processing time has little effect on the material morphology in both UV and heat treatment modes.

Analysis reveals that UV irradiation during soft thermal annealing leads generally to enhancing the evaporation rate of solvents and reducing the film thickness, as well as to forming the folds of smaller transverse sizes.

As shown in Table 1, energy dispersive X-ray (EDX) spectroscopy of the samples during SEM imaging allowed us to determine the Zn/O ratio. It can be seen that in samples prepared using both treatment modes for 90 min, this ratio is almost the same and lies in the range of 0.40–0.45. Increasing the treatment time to 4.5 h leads to an increase in the ratio to 0.87 for samples subjected to combined treatment and to 0.65 for control samples. A change in the Zn/O ratio from 0.5 to 1 during film processing indicates the transition of zinc hydroxide to the oxide phase. At the same time, mild heat treatment, even for 4.5 h, does not result in a complete transition throughout the entire volume of the film.

Figure S1 (see Online Supplementary Materials) depicts the X-ray diffraction (XRD) patterns of all the oxide samples obtained in the study. Their analysis shows that the detected reflections correspond to zinc oxide in the wurtzite crystalline phase (JCPDF 36-1451). In addition, there are reflections corresponding to the families of planes of (100), (002), (101), (102), (110), (103) and (112), as well as one reflection corresponding to the silicon substrate [Si (111)]. Table 1 lists the sizes of coherent scattering regions (nanocrystallites), calculated using the Scherrer equation.[13]

It can be seen that for the samples obtained by combined thermal and UV treatment, the size of nanocrystallites is virtually independent of the treatment time; there is only a slight increase from 24.8 to 26.1 nm. The samples obtained only by moderate thermal annealing without UV irradiation, on the contrary, are characterized by a significant decrease in the size of the coherent scattering regions from 38.6 nm after 1.5 h of treatment to 28.4 nm when treated for 4.5 h. This pattern can be explained in the following way. Probably, during mild heat treatment at 180 °C, the transition of zinc hydroxide into its oxide phase occurs unevenly throughout the entire volume of the film and requires some time. In this regard, due to different cell volumes and lattice parameters of $Zn(OH)_2$ and ZnO, mechanical stresses arise in the material, leading to a decrease in crystallite sizes over time. Presumably, during the first 1.5 h of combined treatment, UV irradiation causes the $Zn(OH)_2 \rightarrow ZnO + H_2O$ transition, which occurs uniformly throughout the entire volume of the film, practically without changing the crystallite size.

Figure S2 presents graphs of $(\alpha E)^2$ *vs.* E (where α is the absorption coefficient and E is the photon energy) for all samples under study. The linear dependence of the functions indicates that all samples are direct-gap semiconductors. Extrapolation of the linear portion of the curve to the intersection with the abscissa axis gives the optical bandgap ΔE_g (see Table 1). It can be seen that

Table 1 Parameters of ZnO samples subjected to various treatments.

Sample	Zn/O[a]	D/nm[b]	$(Zn/O)_{surf}$[c]	$(Zn_{wurtzite}/Zn)_{surf}$[c]	ΔE_g/eV	$E_F - E_C$/eV
90 T	0.40	38.6 ± 0.1	1.40	0.51	3.17 ± 0.01	1.02 ± 0.01
180 T	0.59	34.8 ± 0.1	1.39	0.53	3.19 ± 0.01	0.79 ± 0.01
270 T	0.65	28.4 ± 0.1	1.46	0.50	3.17 ± 0.01	0.57 ± 0.01
90 T+UV	0.45	24.8 ± 0.1	1.46	0.52	3.18 ± 0.01	0.57 ± 0.01
180 T+UV	0.53	25.7 ± 0.1	1.45	0.51	3.17 ± 0.01	0.54 ± 0.01
270 T+UV	0.87	26.1 ± 0.1	1.42	0.53	3.17 ± 0.01	0.62 ± 0.01

[a] According to EDX spectroscopy. [b] According to XRD analysis. [c] According to XPS.

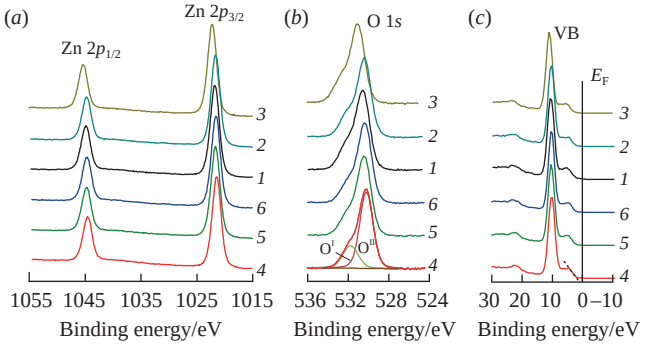

Figure 2 XPS spectra of (*a*) Zn 2*p*, (*b*) O 1*s* and (*c*) valence band in the studied samples (*1*) 90 T, (*2*) 180 T, (*3*) 270 T, (*4*) 90 T+UV, (*5*) 180 T+UV and (*6*) 270 T+UV.

the bandgap in all the samples is almost the same and amounts to 3.17–3.19 eV.

The characteristic features of the chemical composition of the film surface were studied by X-ray photoelectron spectroscopy (XPS). Table 1 summarizes the surface zinc to oxygen ratios for each sample. It was found that the $(Zn/O)_{surf}$ ratio is in the range of 1.39–1.46 and does not show any patterns depending on the treatment conditions. The increased Zn content on the surface is probably caused by etching with the Ar beam, leading to preferential removal of oxygen. Nevertheless, these results indicate a difference in the chemical composition of the surface and bulk of the films. Throughout the entire volume of the film, increasing the treatment time of any type leads to an increase in the Zn/O throughout the film volume, while the surface composition remains relatively stable.

Figure 2 presents the spectra of Zn 2*p* and O 1*s*. The spectrum of zinc [Figure 2(*a*)] is represented by a doublet of Zn $2p_{3/2}$ and Zn $2p_{1/2}$ with binding energies of *ca.* 1021 and *ca.* 1045 eV, respectively. The duration of combined heat and UV treatment does not affect the value of the Zn $2p_{3/2}$ binding energy, and mild heat treatment leads to its enhancement, which indicates an increase in the degree of zinc oxidation. With an almost unchanged $(Zn/O)_{surf}$ ratio, this indicates the release of zinc cations from regular positions and the accumulation of interstitial zinc (Zn_i) in the near-surface region of the films.[14,15]

As shown in Figure 2(*b*), deconvolution of the oxygen O 1*s* spectrum leads to the identification of two components: low-energy O^I with a binding energy of ~530 eV and high-energy O^{II} with a binding energy of ~532 eV. The O^I component corresponds to the O_2^- anion in the wurtzite crystal lattice, and the O^{II} component corresponds to oxygen in hydroxyl groups adsorbed on the surface, as well as in organic residues and other particles not related to ZnO crystals.[16] From the values of the atomic fractions of O^I, it is possible to calculate the fraction of zinc in the films that has converted into the ZnO phase. Since the Zn/O ratio in zinc oxide is 1 : 1, the equation $[O^I] = [Zn_{wurtzite}]$ is valid and the ratio $(Zn_{wurtzite}/Zn)_{surf} = O^I/Zn$ holds. The calculated values are listed in Table 1. Therefore, we can conclude that the fraction of zinc on the surface of the films that transforms into ZnO crystals during the synthesis process is about 50% for all studied samples and this fraction does not depend on the treatment conditions. This result correlates with the stable ratio $(Zn/O)_{surf}$. Thus, the chemical composition of the near-surface region is rather steady, which is apparently due to the balance of the flows of components from the surface of the material into its bulk and into the environment.

Figure 2(*c*) shows the valence band structure estimated in all the samples. Analysis of the sources indicates that deconvolution of the spectrum allows us to identify three components corresponding to Zn 3*d* orbitals, O 2*p* orbitals, hybridized with the Zn 4*s* and Zn 4*p* states, and O 2*p* orbitals.[17] The position of the valence band top

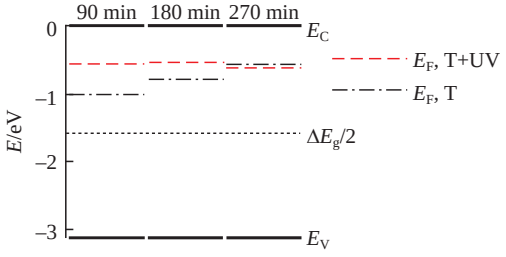

Figure 3 Band energy diagrams of the samples under study.

in the samples was determined by the intersection of the linear portion of the low-energy part of the spectrum with the abscissa axis. Based on the obtained data and bandgap energy values, the Fermi energy level E_F in the samples relative to the bottom of the conduction band E_C was calculated (see Table 1). For clarity, the data are presented as a band energy diagram in Figure 3.

Figure 3 shows that all samples are n-type semiconductors, since the Fermi level in all cases lies closer to the bottom of the conduction band than to the top of the valence band. The duration of combined treatment (T + UV) has virtually no effect on the position of the E_F, which is in the range of 0.54–0.62 eV relative to the E_C. When using only thermal treatment of films, an increase in its time contributes to a monotonic approach of the Fermi level to the bottom of the conduction band in the energy range of 1.00–0.57 eV.

In general, the obtained result correlates with the dependences of the average sizes of film nanocrystallites during their treatment: for both sets of samples, the position of the Fermi level approaches the bottom of the conduction band as the sizes of the coherent scattering regions decrease. During the combined treatment for 1.5–4.5 h, the *D* and $(E_F - E_C)$ values in the films change slightly: as the heat treatment time increases, the crystallite size monotonically decreases and E_F approaches E_C. This is probably due to different degrees of defects in crystallites of different sizes. Since excess defectiveness, not associated with the presence of thermodynamically equilibrium point defects, is concentrated on the surface of single crystals, it should be expected to increase with decreasing nanocrystallite size (~1/*D*). As a rule, such defects are predominantly donors, such as vacancies in the oxygen sublattice V_O and interstitial zinc cations Zn_i.[18] Apparently, a high concentration of donor defects of this kind causes E_F to approach E_C.

The research results have proven the possibility of forming stoichiometric zinc oxide by the sol–gel method, when the annealing procedure was a combination of moderate heat treatment and ultraviolet irradiation. It was shown for the first time that combined treatment with ultraviolet light and heating at 180 °C for 4.5 h provides a Zn/O atomic ratio of 1 : 1, which could not be achieved using only heat treatment at such low temperatures. It was found that the concentration of intrinsic electrically active defects and the position of the Fermi level in the studied ZnO films reach stable values during combined treatment at least three times faster than during moderate heat treatment without ultraviolet irradiation. The results provide a methodology for the formation of semiconductor oxide films by the sol–gel method at low temperatures, relevant for flexible and epidermal electronics using substrates with low melting points. Coatings of this type are promising for the manufacture of gas sensor devices, flexible transistors and tension–compression sensors.

This work was supported by the Russian Science Foundation (grant no. 23-29-00844, https://rscf.ru/project/23-29-00844/). XPS measurements were carried out using the equipment of the Research Park of St. Petersburg State University, ‘Physical methods of surface investigation’.

Online Supplementary Materials

Supplementary data associated with this article can be found in the online version at doi: 10.1016/j.mencom.2024.09.006.

References

1 D.-H. Kim, N. Lu, R. Ma, Y.-S. Kim, R.-H. Kim, S. Wang, J. Wu, S. M. Won, H. Tao, A. Islam, K. J. Yu, T. Kim, R. Chowdhury, M. Ying, L. Xu, M. Li, H.-J. Chung, H. Keum, M. McCormick, P. Liu, Y.-W. Zhang, F. G. Omenetto, Y. Huang, T. Coleman and J. A. Rogers, *Science*, 2011, **333**, 838.

2 W. Zhou, S. Yao, H. Wang, Q. Du, Y. Ma and Y. Zhu, *ACS Nano*, 2020, **14**, 5798.

3 L. Lin, M. Dautta, A. Hajiaghajani, A. R. Escobar, P. Tseng and M. Khine, *Adv. Electron. Mater.*, 2021, **7**, 2000765.

4 W. Gao, S. Emaminejad, H. Y. Y. Nyein, S. Challa, K. Chen, A. Peck, H. M. Fahad, H. Ota, H. Shiraki, D. Kiriya, D.-H. Lien, G. A. Brooks, R. W. Davis and A. Javey, *Nature*, 2016, **529**, 509.

5 H. Lee, C. Song, Y. S. Hong, M. Kim, H. R. Cho, T. Kang, K. Shin, S. H. Choi, T. Hyeon and D.-H. Kim, *Sci. Adv.*, 2017, **3**, e1601314.

6 N. J. Ronkainen, H. B. Halsall and W. R. Heineman, *Chem. Soc. Rev.*, 2010, **39**, 1747.

7 M. A. Shiryaev, S. A. Eremin and A. N. Baranov, *Nanotechnol. Russ.*, 2014, **9**, 99 [*Rossiiskie Nanotekhnologii*, 2014, **9** (3–4), 5].

8 R. D. Munje, S. Muthukumar and S. Prasad, *Sens. Actuators, B*, 2017, **238**, 482.

9 N. P. Shetti, S. D. Bukkitgar, K. R. Reddy, Ch. V. Reddy and T. M. Aminabhavi, *Biosens. Bioelectron.*, 2019, **141**, 111417.

10 A. K. Giri, A. Sinhamahapatra, S. Prakash, J. Chaudhari, V. K. Shahi and A. B. Panda, *J. Mater. Chem. A*, 2013, **1**, 814.

11 E. Casero, M. D. Petit-Domínguez and L. Vázquez, in *Handbook of Sol–Gel Science and Technology*, eds. L. Klein, M. Aparicio and A. Jitianu, Springer, Cham, 2016, chapter: *Enzymatic Sol–Gel Biosensors*.

12 Y.-H. Kim, J.-S. Heo, T.-H. Kim, S. Park, M.-H. Yoon, J. Kim, M. S. Oh, G.-R. Yi, Y.-Y. Noh and S. K. Park, *Nature*, 2012, **489**, 128.

13 U. Holzwarth and N. Gibson, *Nat. Nanotechnol.*, 2011, **6**, 534.

14 I. A. Pronin, I. A. Averin, A. A. Karmanov, N. D. Yakushova, A. S. Komolov, E. F. Lazneva, M. M. Sychev, V. A. Moshnikov and G. Korotcenkov, *Nanomaterials*, 2022, **12**, 1924.

15 A. A. Karmanov, I. A. Pronin, N. D. Yakushova, A. S. Komolov and V. A. Moshnikov, *Inorg. Mater.*, 2022, **58**, 1145 (*Neorg. Mater.*, 2022, **58**, 1184).

16 R. E. Marotti, C. D. Bojorge, E. Broitman, H. R. Cánepa, J. A. Badán, E. A. Dalchiele and A. J. Gellman, *Thin Solid Films*, 2008, **517**, 1077.

17 M. Gabás, S. Gota, J. R. Ramos-Barrado, M. Sánchez, N. T. Barrett, J. Avila and M. Sacchi, *Appl. Phys. Lett.*, 2005, **86**, 042104.

18 A. Janotti and C. G. Van de Walle, *Phys. Rev. B: Condens. Matter Mater. Phys.*, 2007, **76**, 165202.

Received: 4th April 2024; Com. 24/7447